ROYAL SOCIETY
OF CHEMISTRY

Check for updates

Insight into multivalent iron complex-bound oxygen vacancy-rich BiOBr nanodiscs for photocatalytic ammonia synthesis

Vinay Kumar Sriramadasu, [iD] †[a] Himani Joshi, [iD] †[b] Ibamerisha Lyngdoh,[a] Naveen Sharma, [iD] [b] Srimanta Pakhira [iD] *[bc] and Santanu Bhattacharyya [iD] *[a]

Photocatalytic conversion of N_2 to green NH_3 has become extremely promising as an alternative to the traditional Haber–Bosch process for a resilient future. In this context, developing noble metal-free nanomaterials with highly efficient photocatalytic activity is highly demanding. Herein, oxygen vacancy-rich disc-shaped BiOBr (BOB_{OV}) has been synthesized, and a multivalent Fe–phytic acid complex has been further coupled with it to form the final composite – $BOB_{OV}@Fe_x$. It is utilized for photocatalytic NH_3 production from N_2, and further compared with other controlled samples. Detailed structural and elemental properties have been correlated with the intrinsic optoelectronic properties. The results suggest that the coupling of the Fe complex acts synergistically with the oxygen vacancies (OVs), which improve the visible light absorption, charge separation, and N_2 adsorption. It eventually elevates the photocatalytic efficiency. The photocatalytic efficiency for the optimized samples reaches up to 385.5 $\mu M\ g_{cat.}^{-1}\ h^{-1}$ with an AQE of 5.24%. It has been thoroughly supported by a series of computational studies. Quantum mechanical calculations employing the PBE-D method are utilized to provide the crucial role of polyvalent Fe atoms and OVs on the surface of BOB for N_2 activation. Thermodynamic analysis further confirms that the N_2 reduction proceeds most favorably through the associative distal pathway.

Introduction

Ammonia (NH_3), one of the most important chemicals, is extensively used as the main precursor for synthesizing fertilizers, drug molecules, polymers, and other value-added chemicals/important chemical feedstocks in various chemical industries.[1–3] It is also noteworthy that NH_3 has huge potential in renewable energy research as a completely carbon-free liquid energy transporter, due to its higher H_2 content.[4] To date, industries are using the traditional Haber–Bosch process to prepare NH_3 for commercial purposes.[5] However, the traditional Haber–Bosch (HB) process needs extremely harsh conditions to break the completely inert N_2 molecule, which requires high energy and adversely affects the environment by releasing huge amounts of greenhouse gases.[6,7] Furthermore, this method needs highly pure H_2 gas to complete this nitrogen reduction reaction, and the preparation of pure H_2 is another challenging task.[8] In general, this HB process consumes approximately 1–2% of annual global energy and emits ~1.6% of global CO_2 emissions, leading to energy and environmental issues.[9] Therefore, developing an alternative approach for N_2 fixation to NH_3 in a greener, renewable, sustainable, and cost-effective way is extremely crucial and timely.

In this context, the photocatalytic N_2 reduction reaction is gaining special attention due to its promising features.[10,11] In this reaction process, typically a semiconducting material acts as a heterogeneous photocatalyst and can convert N_2 to NH_3 from water in the presence of solar light as the sole energy source.[12] For the first time in 1977, Schrauzer et al. reported nitrogen fixation using rutile TiO_2 as a photocatalyst.[13] Several recent reports have explained the potential applicability of various metal/non-metal-based semiconducting nanomaterials for photocatalytic N_2 activation.[14–18] However, the production efficiency is still extremely low, mainly due to the lack of specific active sites for N_2 adsorption.[19] Additionally, the competitive recombination processes decrease the free carrier migration towards the specific active sites, resulting in the reduction of photocatalytic efficiency.[20] To overcome these challenges, several strategies are commonly adopted that can improve the

[a]*Department of Chemical Sciences, Indian Institute of Science Education and Research (IISER) Berhampur, Berhampur-760010, Odisha, India. E-mail: santanub@iiserbpr.ac.in*

[b]*Theoretical Condensed Matter Physics and Advanced Computational Materials Science Laboratory, Department of Physics, Indian Institute of Technology Indore, Simrol, Khandwa Road, Indore, Madhya Pradesh, 453552, India. E-mail: spakhira@iiti.ac.in; spakhirafsu@gmail.com*

[c]*Theoretical Condensed Matter Physics and Advanced Computational Materials Science Laboratory, Centre for Advanced Electronics (CAE), Indian Institute of Technology Indore, Simrol, Khandwa Road, Indore, Madhya Pradesh, 453552, India*

† Mr Vinay Kumar Sriramadasu and Ms Himani Joshi contributed equally to this manuscript.

overall performance of the photocatalysts, such as defect designing, doping of metal/non-metal heteroatoms, construction of heterostructures, loading of co-catalysts, etc.[4,5,14,21–24]

In a similar context, two-dimensional (2D) semiconducting nanomaterials have gained potential interest as photocatalysts due to their intrinsic anisotropic features, controllable layered structure, thickness-dependent optoelectronic properties, exposed surface-active sites etc.[25–28] 2D bismuth oxyhalide (BOX) is one of the most promising materials in this regard. However, out of all the BOX family members, 2D bismuth oxyhalide (BOB) is the most promising material for photocatalysis due to its strong visible light absorption and efficient stability with respect to other halogen analogues.[8,29] Recently, 2D BOB and/or BOB-based heterostructures have been explored quite substantially as efficient photocatalysts for wastewater remediation, H_2O_2 production, CO_2 conversions to transportable solar fuels, selective organic transformation, etc.[26,30–35] Furthermore, recent reports also explored the potential applicability of BOB for photocatalytic N_2 activation to green NH_3 by controlling the band gap/band positions and oxygen vacancies (OVs).[11,20,23,29,36] In general, OVs in a photocatalyst specifically inhibit the recombination of the photogenerated charges, which is useful for the activation of surface-adsorbed molecules by photocatalysis.[37–39] In the same line, it is also noteworthy that the natural nitrogen fixation process can be an inspiration for designing photocatalysts, where the polyvalent metal centers of the protein molecule play a crucial role as active sites.[5,40] Likewise, incorporation of a selective polyvalent single metal atom into photocatalysts can efficiently boost the photocatalytic N_2 activation.[17] In this regard, the polyvalent iron (Fe) atom is a good choice of metal active sites due to its propensity to chemisorb and activate the inert N_2 gas molecule.[7,27]

In this work, the multi-cationic [Fe(III)/Fe(II)]–phytic acid complex is attached on OV-rich BOB (BOB_{OV}), which has been prepared utilizing phytic acid (PA) as a coordinating molecule. Morphological and elemental features have been investigated by detailed electron microscopy, XRD, and XPS studies. The structural and elemental features have been further correlated with basic optoelectronic properties. This is further supported by electrochemical impedance spectroscopy and transient photocurrent studies. It is noteworthy that the presence of both OVs and polyvalent Fe atoms on BOB synergistically modifies the surface and optoelectronic properties, resulting in enhanced adsorption of N_2 molecules on homogeneously dispersed active sites and eventually their photoreduction to NH_3. To supplement the experimental results, a detailed computational study has been employed to gain an in-depth understanding of the photocatalytic nitrogen reduction on $BOB_{OV}@Fe_x$. Our computed results show that the presence of the Fe atom along with OV formation effectively modulates the electronic properties of BOB, resulting in superior N_2 activation and enhanced photocatalytic NH_3 generation. Thermodynamic analysis further confirms that the nitrogen reduction proceeds most favorably through the associative distal pathway on the $BOB_{OV}@Fe_x$ system. Additionally, Fe provides additional active sites to enhance the N_2 activation capacity towards reduction reactions and enhance the overall catalytic performance of

$BOB_{OV}@Fe_x$, which is in accordance with the experimental observation.

Results and discussion

OVs-rich and Fe(III)/Fe(II)-complex anchored BOB material, i.e., $BOB_{OV}@Fe_x$, was synthesized by the in situ growth of BOB in the presence of the Fe–phytic acid complex (Fe–PA) through a facile solvothermal approach. Here, PA has the roles of coordinating multi-valent metal cations and serving as a molecular bridge with the BOB substrate material.[41,42] This specific methodology will be beneficial for obtaining homogeneously distributed, aggregation-free metal sites as active centers on the base photocatalyst. The detailed synthesis process is explained in the Experimental section. First, Fe–PA was prepared by the traditional method of mixing PA and $Fe(NO_3)_3$ in a molar ratio of 1 : 6. Herein, six Fe atoms were bound to the six phosphate groups of one chelating PA molecule to form the Fe–PA complex.[43] Afterwards, in the presence of Fe–PA powder (used amount (x) = 2, 3, 5, 7.5, 10 mg), BOB_{OV} was synthesized in situ to obtain the final material (i.e., $BOB_{OV}@Fe_x$). Similarly, pristine BOB_{OV} was also prepared using the same synthesis route in the absence of Fe–PA. Pure BiOBr without OVs (BOB) was obtained by calcining the BOB_{OV} in an open O_2 atmosphere.

The crystalline structure of the materials has been analyzed by X-ray diffraction (XRD) studies. From the XRD patterns of BOB and BOBov, the sharp intense peaks positioned at 11.94°, 22.94°, 26.18°, 32.70°, 33.22°, 40.3°, 47.18° and 58.06° are assigned to the (001), (002), (101), (102), (110), (112), (020), and (212) planes of BOB (JCPDS no. 85-0862) (Fig. 1a).[44] The dominance of the (102) plane is clearly noticeable. Upon anchoring polyvalent Fe atoms on the BOB surface (for $BOB_{OV}@Fe_5$), the diffraction pattern remained almost unaltered, which suggests no formation of a new material. However, slight broadening of all the diffraction peaks is attributed to the minimal distortion in the crystallinity of BOB caused by the presence of residual stress originating from Fe–PA.[45] A reduction in the peak intensity corresponding to the (102) plane is observed, which is mainly because of the presence of Fe–PA on the exposed plane of BOB, i.e., plane (102).

Additionally, field emission scanning electron microscopy (FE-SEM) and transmission electron microscopy (TEM) have been employed to reveal the morphological & structural features of the materials, respectively. From the FE-SEM images, the pristine BOB_{OV} shows a square-shaped nanoplate morphology, whereas $BOB_{OV}@Fe_5$ possesses a slightly irregular circular disc-like morphology (Fig. 1b and c). These morphological changes are in accordance with the obtained XRD data. This is further clarified by TEM images. The TEM images of BOB_{OV} and $BOB_{OV}@Fe_5$ have been depicted in Fig. 1d and e, respectively. The HR-TEM images of pristine BOB_{OV} show uniform and clear lattice fringes with a calculated d spacing of 0.281 nm (Fig. S1). This can be assigned to the (102) plane of BOB_{OV}.[35] The SAED pattern (depicted in the inset image of Fig. S1) further suggests the highly crystalline nature of BOB_{OV}. As shown in Fig. 1f, the d-spacing value of $BOB_{OV}@Fe_5$ remains unaltered, which further suggests that Fe-loading doesn't affect the crystal nature
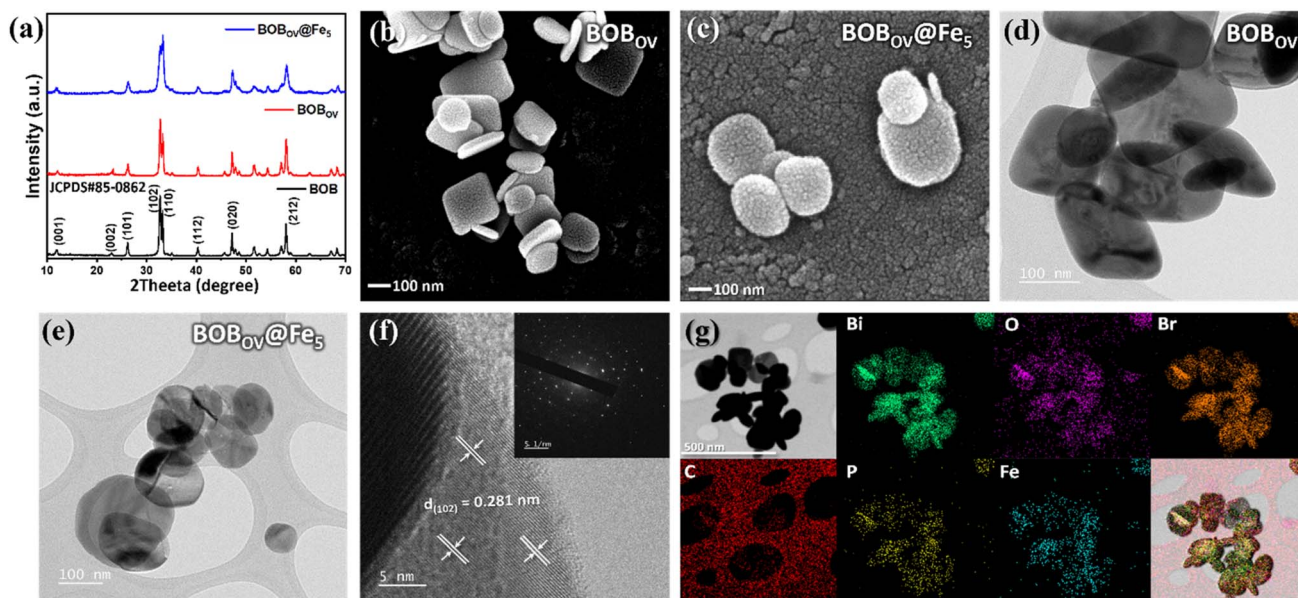
Paper   Journal of Materials Chemistry A

Fig. 1 (a) XRD patterns of BOB, BOB$_{OV}$, and BOB$_{OV}$@Fe$_5$. FE-SEM images of (b) BOB$_{OV}$ and (c) BOB$_{OV}$@Fe$_5$. TEM images of (d) BOB$_{OV}$ and (e) BOB$_{OV}$@Fe$_5$, respectively. (f) HR-TEM image (inset image: SAED pattern) and (g) EDX elemental mapping of BOB$_{OV}$@Fe$_5$.

of pristine BOB$_{OV}$. The SAED pattern further supports this (inset of Fig. 1f). EDX elemental mapping has been employed to determine the presence of the constituent elements and their distribution over the materials (Fig. S2 and 1g). Specifically, the homogeneous distribution of elements 'P' and 'Fe' in BOB$_{OV}$@Fe$_5$ clearly suggests the proper distribution of Fe-atoms over the material (Fig. 1g).

The constituent elements of the materials and their valence states have been studied by X-ray photoelectron spectroscopy (XPS), and the recorded spectra are depicted in Fig. 2a–e. From the survey spectra of BOB$_{OV}$, the signals located at binding energies of ~160, 530, 284, and 68 eV, have been assigned to Bi 4f, O 1s, C 1s, and Br 3d, respectively (Fig. 2a). In addition to these peaks, the survey spectra for BOB$_{OV}$@Fe$_5$ contain two more peaks situated at ~134 and 710 eV, which correspond to the elements P 2p and Fe 2p, respectively.[46,47] This confirms the existence of all the elements of the material. For an in-depth study, high-resolution XPS spectra of each element have been employed. Fig. 2b shows the comparative high-resolution XPS spectra of Bi 4f for BOB$_{OV}$@Fe$_5$ (depicted in the upper panel) and BOB$_{OV}$ (depicted in the lower panel). For the pristine BOB$_{OV}$, the two strong bands centered at 159.15 and 164.44 eV are assigned to Bi 4f$_{7/2}$ and 4f$_{5/2}$, respectively. These two signals suggest the +3-oxidation state of Bi.[11,35] In the case of BOB$_{OV}$@Fe$_5$, the same peaks are shifted slightly to higher binding energy values of 159.38 and 164.67 eV, respectively. This suggests the possible electron redistribution between Bi and Fe metals in the final system.[27]

The high-resolution O 1s XPS spectra for BOB$_{OV}$ have been deconvoluted into three peaks, which are present at 529.84, 531.16, and 531.90 eV, respectively (Fig. 2c). These three characteristic peaks can be assigned to lattice oxygen (O$_{Latt.}$), oxygen vacancies (OVs), and adsorbed oxygen (O$_{Ads.}$), respectively.[21,37] The same deconvoluted peaks are observed for BOB$_{OV}$@Fe$_5$ at

530.09, 532.10, and 532.31 eV, respectively. In addition, an increase in the area under the 'OVs' peak is correlated with the existence of higher oxygen vacancies in the final material. High-resolution XPS spectra of Br 3d have been deconvoluted into two peaks (depicted in Fig. 2d). The deconvoluted peaks are identified as Br 3d$_{5/2}$ and 3d$_{3/2}$, located at 68.07 and 69.14 eV for BOB$_{OV}$, and 68.18 and 69.23 eV for BOB$_{OV}$@Fe-5, respectively.[26]

Furthermore, high-resolution XPS spectra of Fe 2p and P 2p have been employed for BOB$_{OV}$@Fe$_5$. Fig. 2e shows the Fe 2p spectra; the signals situated at 710.81 and 723.84 eV are assigned to Fe 2p$_{3/2}$ and 2p$_{1/2}$, respectively.[48] This confirms the presence of Fe with both oxidation states (2+/3+). High-resolution XPS spectra of P 2p have a strong signal at 134 eV, which originates from PA. Upon deconvolution, the peaks positioned at 133.46 and 134.13 eV were identified as P 2p$_{3/2}$ and 2p$_{1/2}$, respectively, suggesting the oxidation states of phosphorus.[49]

The electron paramagnetic resonance (EPR) technique has been used to confirm and quantify the OVs in the materials. The signals with a g-value of 2.003 indicate the presence of OVs in all these materials (Fig. 2f).[36,50] The intensities of the signals express the concentrations of OVs within the materials. BOB$_{OV}$ has more OVs than the pristine BOB, and the final material has the highest concentration of OVs. Anchoring polyvalent metal atoms on BOB$_{OV}$ could improve the defects in the system. The introduction of the foreign atom/molecule alters the structural and electronic properties of the pristine BOB. To compensate for these changes, bonds attached with nearby oxygen atoms become weak, resulting in the creation of OVs.[24,39] These results are well-matched with the analyzed XPS O 1s spectral information. Furthermore, the specific surface area (SSA) of the materials has been determined through BET-N$_2$ adsorption–desorption isotherms (Fig. S4). The enhanced SSA of the BOB$_{OV}$ and BOB$_{OV}$@Fe$_5$ is greater than that of BOB.
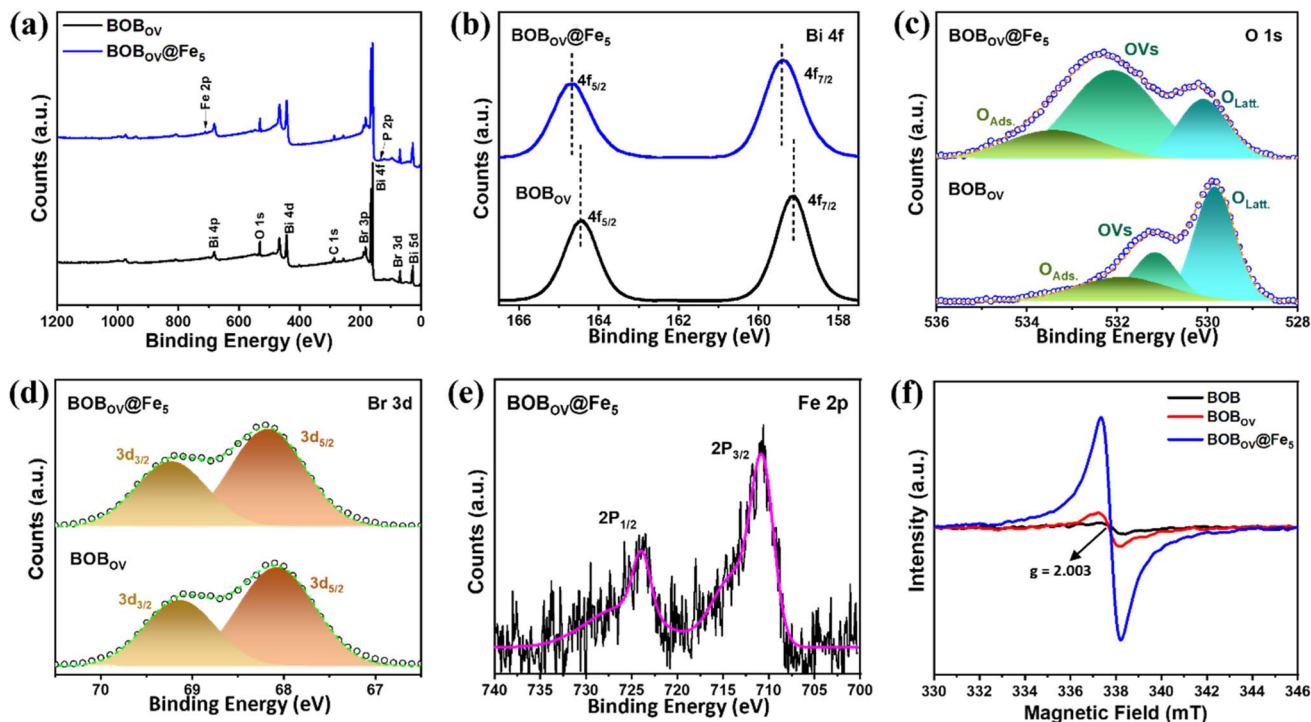
Fig. 2 (a) XPS survey spectra and comparative high-resolution XPS spectra of (b) Bi 4f, (c) O 1s, and (d) Br 3d for BOB$_{OV}$ and BOB$_{OV}$@Fe$_5$, respectively. (e) High-resolution XPS Fe 2p spectra of BOB$_{OV}$@Fe$_5$. (f) EPR spectra for BOB, BOB$_{OV}$, and BOB$_{OV}$@Fe$_5$.

The absorption properties of the materials were examined by DRS UV-vis absorbance spectroscopy (Fig. 3a and S5a). Compared to the pristine BOB, the presence of OVs increases the visible light absorption in BOB$_{OV}$.[29] Furthermore, the gradual loading of Fe–PA in the final materials (BOB$_{OV}$@Fe$_x$) enhances the absorbance in the visible region (Fig. S5a). 'Tauc plots' are made by using the modified K–M function to determine the bandgap energy (E_g) values of the materials.[26] The
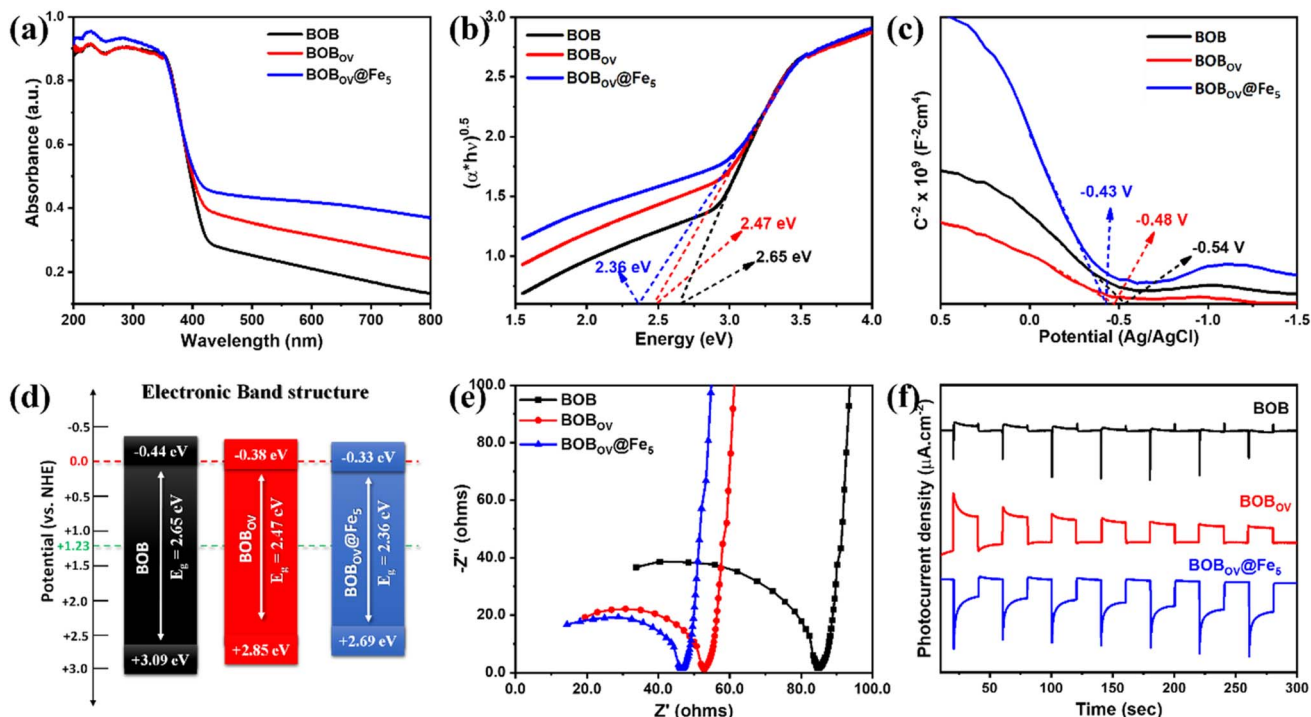

Fig. 3 (a) DRS UV-vis absorbance spectra, (b) Tauc plots, (c) M−S curves, (d) schematic representation of electronic band structures, (e) EIS-Nyquist plots, and (f) transient $I–t$ responses for BOB, BOB$_{OV}$, and BOB$_{OV}$@Fe$_5$.

plotted Tauc plots are shown in Fig. 3b, and the calculated E_g values are 2.65, 2.47, and 2.36 eV for BOB, BOB_{OV}, and $BOB_{OV}@Fe_5$, respectively. The reduction in the bandgap energy of $BOB_{OV}@Fe_5$ is attributed to the synergistic effect of OVs and the presence of Fe-atoms. The improved light absorption will promote higher photocatalytic activity of the final material than the pristine samples.[11] PL spectra and TRPL spectra (with the fitted curves) are depicted in Fig. S5b and c. The determined average lifetime (τ) values are 0.78, 0.70, and 0.31 ns for BOB, BOB_{OV}, and $BOB_{OV}@Fe_5$, respectively. These results suggest that the effective separation of the photo-induced charges is enhanced by OVs in BOB_{OV} with respect to the pristine BOB system, and it is further improved by the metal sites in $BOB_{OV}@Fe_5$.[21]

Mott–Schottky (M–S) curves are recorded to determine the semiconducting nature as well as the flat band potentials (E_{fb}) of the photocatalysts. The recorded M–S plots are presented in Fig. 3c, and the positive slope for all the materials indicates their n-type semiconducting behavior.[32] The E_{fb} values are determined from the tangential intercept of the curves, and these values are −0.54, −0.48, and −0.43 V ($vs.$ Ag/AgCl) for BOB, BOB_{OV}, and $BOB_{OV}@Fe_5$, respectively. The calculated E_{fb} values are −0.343, −0.283, and −0.233 V (with respect to NHE) for BOB, BOB_{OV}, and $BOB_{OV}@Fe_5$, respectively.[51] For n-type materials, the conduction band position (E_{CB}) can be expected to be ∼0.1 V above E_{fb}.[52] Therefore, the E_{CB} values of BOB, BOB_{OV}, and $BOB_{OV}@Fe_5$ are expected at the potentials of −0.44, −0.38, and −0.33 V ($vs.$ NHE), respectively. From the equation $E_{VB} = E_g − E_{CB}$, the valence band positions (E_{VB}) are determined to be +3.09, +2.85, and +2.69 V ($vs.$ NHE) for BOB, BOB_{OV}, and $BOB_{OV}@Fe_5$, respectively. The estimated electronic band structure of these photocatalysts are pictorially represented in Fig. 3d. A conclusion can be drawn that all these materials have sufficient bandgap energy with suitable CB and VB positions to reduce N_2 and oxidize H_2O. To study the (photo)electronic behavior of these materials, EIS Nyquist and transient photo–current (I–t) studies were conducted. In the Nyquist plot, the smaller arc size in the high frequency region represents the higher conductivity of the material.[38,39,53] In comparison to pure BOB, BOB_{OV} has lower impedance, which supports the presence of OVs in it (Fig. 3e). The electronic conductivity is further improved for the final sample, $i.e.$, $BOB_{OV}@Fe_5$. This phenomenon suggests that surface-bound Fe(III)/Fe(II) atoms facilitate the overall charge separation process. The photoactivity of these materials was further examined by recording the current responses under repeated light and dark conditions (for 20 seconds each). The results suggest that the maximum photo-current density is observed for $BOB_{OV}@Fe_5$ and the least for pristine BOB (Fig. 3f). In addition, the steady increase in the photocurrent intensity for $BOB_{OV}@Fe_5$ indicates its better photoactivity for photocalysis reactions.

The equilibrium geometries of the pristine BOB, BOB_{OV}, and $BOB_{OV}@Fe_x$ materials were obtained by the PBE-D method in the present investigation, as depicted in Fig. 4a–k.[54–56] Electronic properties, $i.e.$, the electronic band structure, total density of states (TDOS), electronic band gap (E_g), and partial density of states of these materials were calculated by employing the B3LYP-D method implemented in the CRYSTAL23 suite code.[57] The detailed computational methods employed in this study are provided in the SI. The electronic bands are plotted along the highly symmetric k-path Γ–R–N–Γ in the first Brillouin zone, consistent with the symmetry of the subject material. We have plotted a total of 8 spin-up (4 valence and 4 conduction) bands as depicted in Fig. 4b. The pristine 2D BOB system has a direct electronic band gap (E_g) of 3.2 eV at the point Γ, which reveals that the 2D BOB is a wide band gap semiconducting material as shown in Fig. 4b and c. Furthermore, the equilibrium structure of the OV variant of the BOB system (BOB_{OV}) is depicted in Fig. 4d. BOB_{OV} shows a direct electronic band gap of ∼2.4 eV at the point Γ, as represented in the band structure calculation in Fig. 4e, and the DOS of BOB_{OV} is depicted in Fig. 4f, which further confirms its semiconducting nature. It should be noted here that the oxygen vacancies in the pristine BOB reduce the electronic band gap of the subject material by 0.80 eV, as computed by the B3LYP-D method.

To reveal the significant roles of the bound iron atoms and OVs on the surface of $BOB_{OV}@Fe$, a simplest model material was designed for the final system, and it is depicted in Fig. 4g. The equilibrium structure of the $BOB_{OV}@Fe_x$ materials is depicted in Fig. 4g, and their electronic band structures along with the density of states are displayed in Fig. 4h and i. In the Fe-doped BOB_{OV} system, $BOB_{OV}@Fe_x$, it has been found that the valence band maxima overlap with the Fermi energy level (E_F) along with a significant electron density of states, as depicted in Fig. 4i. This is primarily due to the overlap of the 3d orbital of Fe with the 2p orbital of the O atom, creating impurity states above the VBM, which can be further verified by the plotted partial density of states (PDOS) of Fe '**d** orbitals' and O '**p** orbitals' (Fig. 4j and k). The modification of the electronic structure of BOB through chemically bound transition metals and OVs significantly enhances photocatalyst stability and activity by promoting adsorbed species activation and internal electron transfer. The synergistic interaction between the surface bound metal centres (here Fe) and OVs enables efficient visible-light-driven nitrogen fixation through improved charge carrier dynamics.[58] Thus, our results reveal that the Fe-cation loaded BOB monolayer with OVs shows excellent conducting nature with a high electronic density available around the E_F. This will be highly beneficial for photocatalytic reactions. The computed electronic band gap values fall within the optimal range for efficient photocatalytic activity and correlate well with the experimentally observed band gaps of the subject materials considered in the present investigation.[32]

Photocatalytic NH_3 production from N_2 reduction

Based on the above-analyzed data, all the materials have been utilized for photocatalytic N_2 activation using a customized commercial white LED strip-based light source at room temperature. The photocatalytic activity under a commercially available LED source suggests the practical applicability of the present system. A saturated N_2 gas atmosphere serves as the source for the photocatalytic nitrogen fixation. The complete
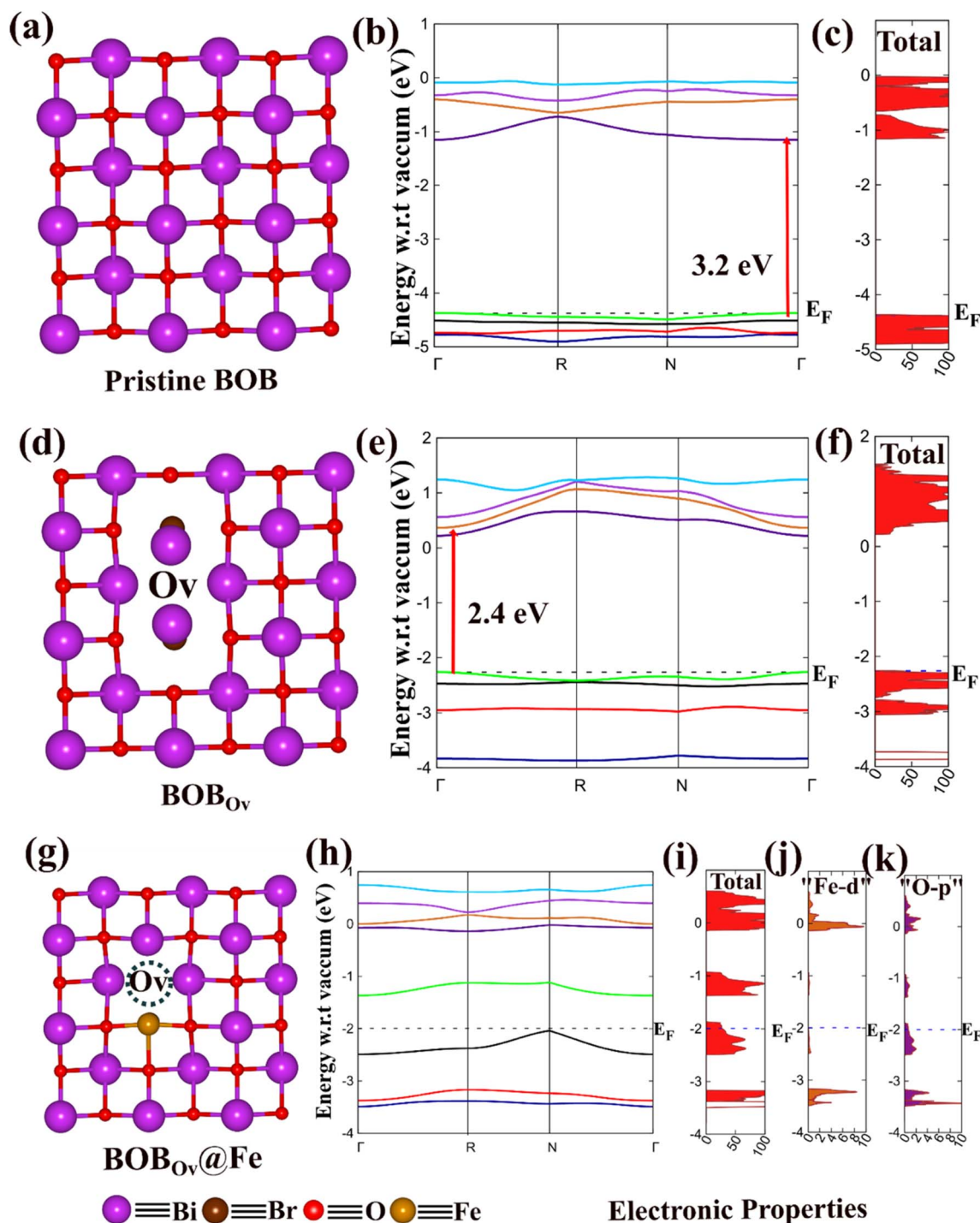
Fig. 4 The equilibrium structures and electronic properties of pristine BOB, BOB_{OV}, and $BOB_{OV}@Fe_x$. The optimized structure, electronic band structure, and density of states of (a–c) BOB, (d–f) BOB_{OV}, and (g–i) $BOB_{OV}@Fe_x$, respectively. Partial DOS of (j) Fe-d orbitals and (k) O-p orbitals of $BOB_{OV}@Fe_x$.

photocatalytic reaction procedure is explained in the Experimental section. A well-established indophenol method has been employed to quantify the ammonia produced in the photocatalytic reactions.[38] In this method, the characteristic absorption peak of the formed indophenol complex at 698 nm is utilized for the quantitative estimation of NH_3.[59] For this, a standard calibration curve was prepared by plotting a series of

known concentrations of ammonia solutions on the x-axis *versus* their respective optical densities (OD) on the y-axis (Fig. S6). The OD values are in a good linear relationship with the concentrations of NH_3 ($R^2 = 0.9975$). Similarly, the possible formation of the by-product (*i.e.*, N_2H_4) during the photocatalytic production of NH_3 is determined by the Watt–Chrisp method.[22] A standard curve has been prepared from the known

concentrations of N_2H_4, and the plotted graph is depicted in Fig. S7. The photocatalytic reaction conditions were optimized in the presence of 1 v/v% aqueous CH_3OH (Fig. 5a).[37] CH_3OH acts as a hole scavenger to donate H^+ through the H_2O oxidation reaction.[53] Furthermore, NH_3 produced through photocatalysis has been confirmed by NMR and HR-MS studies. After the completion of the photocatalysis reaction, the product was initially identified by ^1H NMR in DMSO-d6 solvent. The triplet peaks in ^1H NMR at 7.04, 7.16, and 7.29 ppm clearly confirm the formation of NH_3 (as depicted in Fig. S8).[17,50] It is further confirmed by mass spectroscopy. The single intensified signal at $m/z = 297.05$ indicates the formation of the complex between indophenol dye and NH_3 (Fig. S9).[22] No production of NH_3 was detected under dark and without-photocatalyst conditions, confirming that this reaction is a completely photocatalytic process.

Fig. 5b depicts the optimum NH_3 production rates obtained by using all the as-synthesized photocatalysts. Compared to pure BOB, the photocatalytic activity of BOB_{OV} is increased, which can be attributed to the significant role of OVs in it. The surface oxygen defects in the material are helpful for the adsorption and activation of the N_2 gas molecules.[36] The production rates for the Fe-atom bound composites, *i.e.*, $BOB_{OV}@Fe_x$, show that the maximum NH_3 production rate reached up to 385.5 μM $g_{cat.}^{-1}$ h^{-1} for $BOB_{OV}@Fe_5$. The enhanced NH_3 production is attributed to the Fe atoms that are bound through the chelating molecule on the BOB_{OV}. No NH_3 production is observed for the pure Fe–PA, confirming that only the bound multivalent iron atoms on BOB_{OV} play the role in

reducing N_2. Furthermore, the mandatory roles of H_2O and N_2 gas in N_2 activation were investigated by modifying the reaction conditions: using acetonitrile (ACN) as the solvent medium and saturated 'Ar' & an ambient open atmosphere instead of N_2 (Fig. 5c). Negligible production of NH_3 is observed in these reactions, suggesting that H_2O acts as a proton source, and the purged N_2 is a reactant source for the photocatalytic N_2 fixation.[19,29] In the same context, the reduction of N_2 by the photocatalysts was further confirmed by transient $I–t$ studies performed under saturated Ar/N_2 atmospheres (Fig. 5d). The resulting low photocurrent density value in the saturated N_2 atmosphere with respect to the saturated Ar atmosphere can be attributed to the interaction between photogenerated electrons (e^-) and N_2 gas molecules.[14,51] This difference in photocurrent densities in different atmospheres is highest for $BOB_{OV}@Fe_5$ compared to BOB_{OV} and BOB, which clearly confirms that the final material is more prone to interactions with N_2 gas, which eventually improves the photocatalytic N_2 activation.

To gain insight into the individual roles of P-free carbon content, P-containing carbon (*i.e.*, PA), and Fe-atoms anchored on the BOB surface, a few additional controlled samples have been explored further. These are $BOB_{OV}@C$, $BOB_{OV}@PA$, and $BOB_{OV}@Ni_5$. The synthesis details are provided in the Experimental section, SI. The photocatalytic NH_3 production rates of these controlled samples are depicted in Fig. 5e. It is observed that the photocatalytic efficiencies of $BOB_{OV}@C$ and $BOB_{OV}@$-PA are higher than that of pristine BOB_{OV}. This is probably due to the improved charge transport by the carbon-based material attached to BOB_{OV}.[30] It is also noteworthy that the
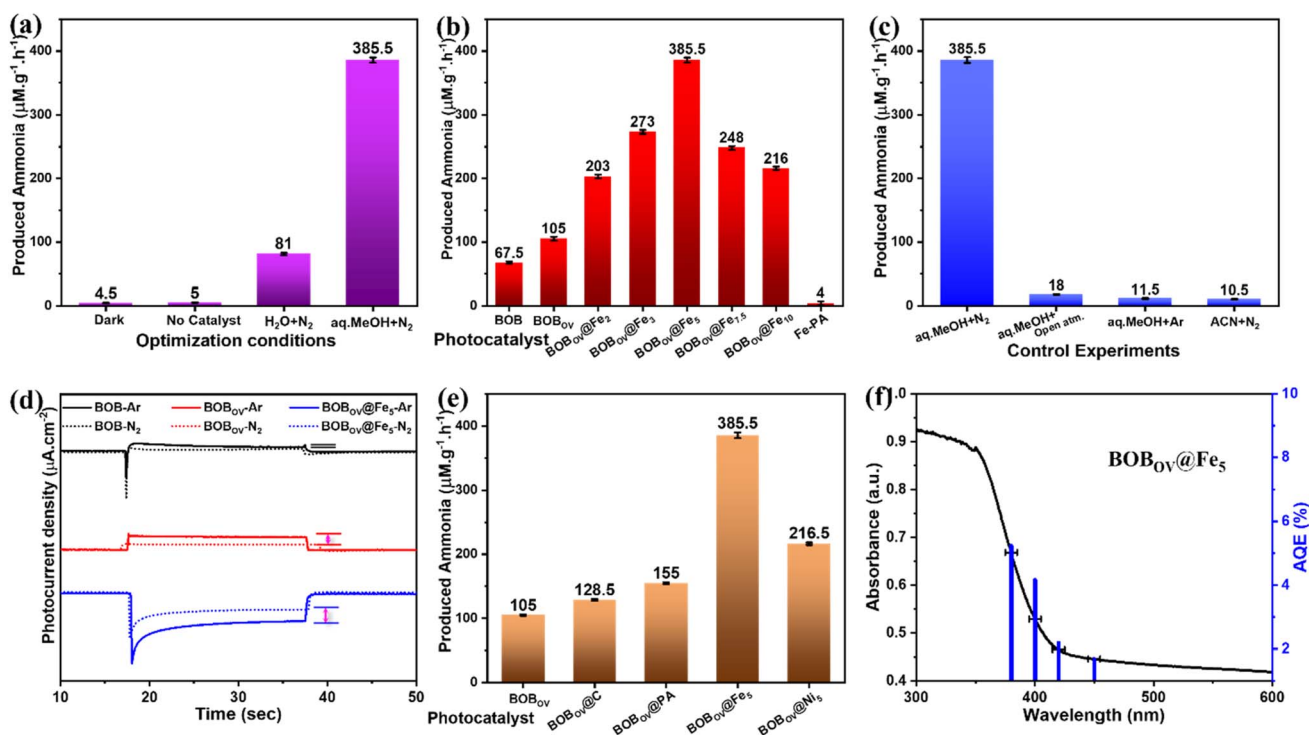

Fig. 5 (a) Optimization of photocatalytic reaction under various conditions, (b) photocatalytic N_2 reduction by different photocatalysts, (c) control experiments for photocatalysis, (d) photocurrent responses of BOB, BOB_{OV}, and $BOB_{OV}@Fe_5$ under sat. Ar/N_2 conditions, (e) influence of active sites on photocatalytic reduction, and (f) plot of AQE (%) *vs.* absorbance spectra of $BOB_{OV}@Fe_5$.

photocatalytic efficiency of $BOB_{OV}@Ni_5$ (similar Ni source, *i.e.*, the Ni-PA precursor) is lower than that of our final composite $BOB_{OV}@Fe_5$. This indirectly suggests the vital role of 'Fe' as an active site for N_2 activation.[48] All the recorded absorption spectra for the indophenol tests are depicted in Fig. S10. In addition, the photocatalytic activity of BOB, BOBov, and $BOB_{OV}@Fe_5$ using a 300 W Xe light source (with full spectra) has been depicted in Fig. S11. The similar trends, with minimal differences in production rates of the materials, demonstrate the real-time utility of these photocatalysts.

Furthermore, the Watt–Chrisp method was employed to determine the formation of the major intermediate, N_2H_4, during photocatalytic NH_3 synthesis (Fig. S12), and no trace of N_2H_4 was detected in the reaction. The absence of N_2H_4 confirms that $BOB_{OV}@Fe_5$ follows the associative distal pathway of nitrogen reduction reaction to produce NH_3.[27]

Based on the above-mentioned analysis, the following key points are listed to propose a possible mechanism of photocatalytic N_2 fixation to NH_3 on $BOB_{OV}@Fe_5$: (i) the higher specific surface area with larger oxygen vacancies in $BOB_{OV}@$-Fe_5 will help to increase the photocatalytic activity. The SSA is utilized to accumulate more N_2 molecules, and surface OVs (*i.e.*, trapping agents of electrons) increase the reduction of adsorbed reactant molecules.[8,50] (ii) The enhanced visible light absorbance and transport of photo-induced charge carriers will contribute more charges to enhance the redox reaction during photocatalysis.[23] (iii) Importantly, the photocatalyst, $BOB_{OV}@$-Fe_5, has strong reduction and oxidation potentials, *i.e.*, the CB and VB are at −0.33 and 2.69 eV (*vs.* NHE), respectively. The alignment of these band potentials is well-suited for the photocatalytic NH_3 synthesis from N_2 reduction. (iv) Specifically, the chemically attached metallic Fe atoms with multiple oxidation states on BOB_{OV} play a crucial role in effective charge separation and the adsorption and activation of the N_2 molecules during the reaction. All these features of the final photocatalyst make it an efficient photocatalyst for the photocatalytic fixation of N_2, and it is schematically represented in Fig. S13.

Furthermore, the photocatalytic efficiency of $BOB_{OV}@Fe_5$ has been examined at various wavelengths (λ) of light. The photocatalytic production rates of NH_3 are 125, 329.5, 145, and 120 μM $g_{cat.}^{-1}$ h^{-1} under 380, 400, 420, and 450 (±5) nm wavelengths, respectively. The calculated apparent quantum efficiency (AQE) values are 5.24, 4.17, 2.195, and 1.69% for 380, 400, 420, and 450 (±5) nm wavelengths, respectively. A plot of the calculated AQE (%) values *vs.* absorbance spectra of $BOB_{OV}@Fe_5$ has been depicted in Fig. 5f. The stability of the photocatalyst was examined by cyclic stability tests (Fig. S14a). In comparison to the first cycle, 64.46% of the NH_3 yield is obtained even in the 5th cycle. After five consecutive cycles of photocatalysis, the used photocatalyst is considered for XRD analysis to observe the modifications (Fig. S14b). No changes are observed in the pattern, suggesting the stability of the photocatalyst. Fig. S14c shows the DRS absorbance spectra of the used photocatalyst. Even after several photocatalytic reduction reactions, the visible light absorbance spectra remain unaltered. The post-reaction elemental studies have been carried out through XPS measurements, which further confirm

the stability of the photocatalysts (Fig. S15). However, a slight decrease in areal OVs (%) clearly suggests the direct involvement of OVs in the photocatalysis process (Table S1).[22] The photocatalytic NH_3 production efficiencies of these materials have been further compared with those of other reported photocatalysts in a tabular form and depicted in Table S2.

To explore the reaction mechanisms of N_2 reduction using the PBE-D method (in short, the DFT method), here we have determined the change in Gibbs free energy (ΔG) of various reaction intermediates formed during the reaction with the help of eqn (S2). In the photocatalytic N_2 reduction reaction, the successive proton-coupled electron transfer (PCET) reactions happen on the surface of the catalyst. We have explored both associative distal and associative alternating reaction pathways toward N_2 reduction on the surface of the $BOB_{OV}@Fe_x$ material and reported the value of ΔG in the case of each reaction intermediate involved in the N_2 activation. Fig. 6 and S16 represent the equilibrium structures of all the reaction intermediates involved in the associative distal and associative alternating reaction pathways, respectively.

We have calculated the values of ΔG or relative free energy (eV) with respect to the N_2 intermediate formation as a reference geometry. Fig. 7a and b presents the free energy diagram (also known as the potential energy surface (PES) profile) for both the associative distal and associative alternating pathways for N_2 reduction on the surface of the $BOB_{OV}@Fe_x$ material. In the case of both the associative distal and alternating pathways, all the reaction steps involved in N_2 reduction are exothermic, and proceed downhill, except for the step in which the last molecule of NH_3 is produced, which is an endothermic reaction step. However, the computed values of ΔG during the NH_3 formation are −1.85 eV and −0.85 eV with respect to the previous step during the associative distal and alternating reaction pathways. As illustrated in Fig. 7, the first NH_3 molecule is released readily, as NH_3 desorption is exothermic in both cases. However, the evolution of the second NH_3 molecule requires external energy input. A critical difference emerges between the pathways: the *NNH → *NNH_2 step in the associative distal pathway is significantly more downhill compared to the *NNH → *NH_NH step in the associative alternating pathway. This step represents the primary distinguishing factor between the two pathways, demonstrating that the *NNH → *NNH_2 reaction pathway is more exothermic and that the intermediate *NNH_2 forms more readily than the intermediate *NH_NH. Consequently, the associative distal pathway is more thermodynamically favourable for NH_3 formation compared to the associative alternating pathway that takes place on the surface of $BOB_{OV}@Fe_x$. The desorption the second NH_3 molecule is the rate-limiting step in the whole N_2 reduction reaction process based on the calculated relative free energies as depicted in Fig. 7a and b. We observed that the photocatalytic N_2 activation on the surface of the $BOB_{OV}@Fe_x$ material demonstrates superior performance compared to previously reported materials, including the Cu-doped BiOBr catalyst.[60]

Additionally, we observed that the N–N bond length slightly increased from 1.10 Å to 1.14 Å after the adsorption of the N_2 molecule at the Fe active site of $BOB_{OV}@Fe_x$. This is due to more
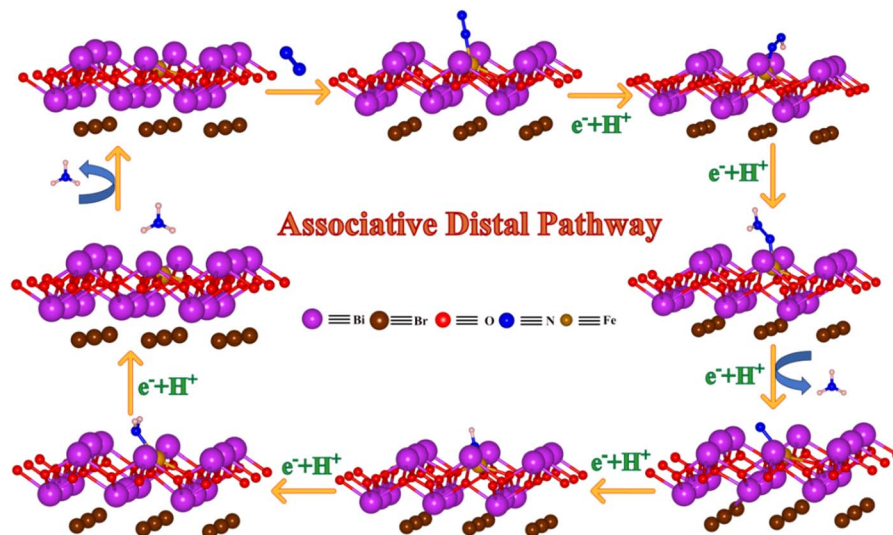
Fig. 6 Equilibrium structures of the reaction intermediates involved in the associative distal pathway of the N_2 reduction reaction on the surfaces of $BOB_{OV}@Fe_x$ obtained by the PBE-D method.

charge transfer from the $BOB_{OV}@Fe_x$ system to the N_2 molecule when it is adsorbed at the Fe active site.[8] The elongation can be attributed to a substantial charge transfer from the $BOB_{OV}@Fe_x$ system to the N_2 molecule when it is adsorbed at the Fe site near the O-vacancy. To visualize this charge transfer, we have shown here charge difference density results in Fig. 7c. For N_2 adsorption on the surface of $BOB_{OV}@Fe_x$, we observed higher charge localization near the N_2 molecule as depicted in Fig. 7c. This localized charge distribution confirms the enhanced charge transfer from the $BOB_{OV}@Fe_x$ system to the N_2 molecule when adsorbed at the

Fe site near the oxygen vacancy. This charge transfer weakens the N–N bond, thereby enhancing N_2 molecule activation for the subsequent photocatalytic N_2 reduction reaction.[22] Based on both theoretical and experimental results, the superior nitrogen reduction to ammonia production on the surfaces of $BOB_{OV}@Fe_x$ can be attributed to two key factors: chemically bound polyvalent Fe-atoms and OVs. The enhanced photocatalytic activity results from the increased surface defects, which facilitate N_2 molecule adsorption while reducing charge carrier recombination. Furthermore, the combined theoretical and experimental study
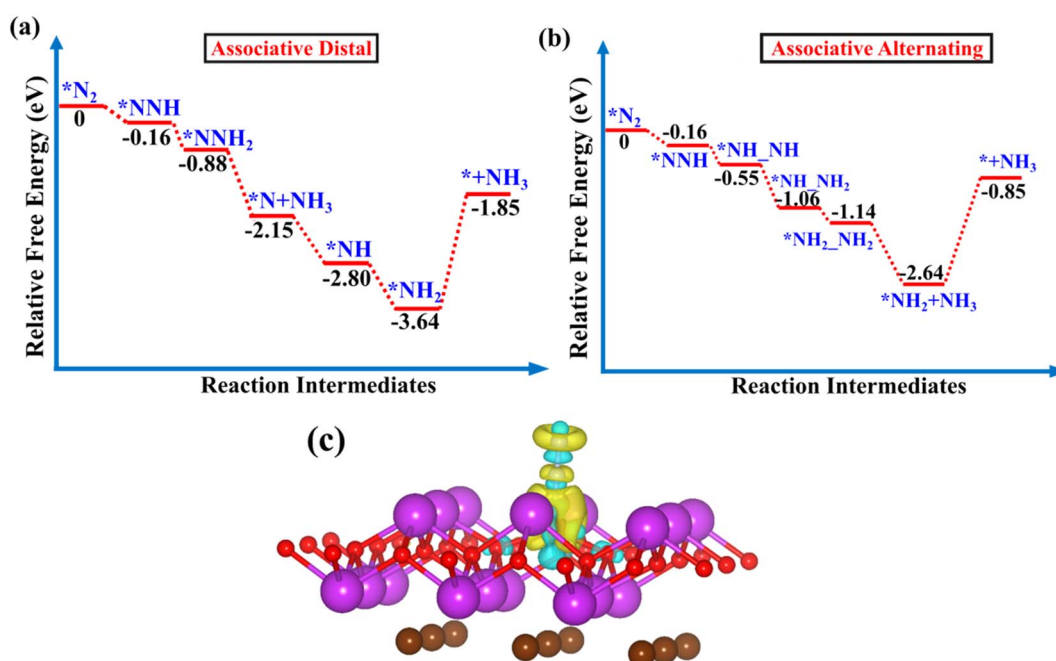

Fig. 7 Free energy diagram or potential energy profiles of the NRR on $BOB_{OV}@Fe_x$ obtained by the PBE-D method. (a) Associative distal pathway, and (b) associative alternating pathway. (c) Charge density analysis of the N_2 adsorbed on the surface of the $BOB_Ov@Fe_x$ system. Here, the yellow colour represents charge accumulation and the cyan colour represents charge depletion).

confirms that the NH_3 formation proceeds *via* the associative distal pathway, establishing this as the preferred nitrogen reduction reaction mechanism for the $BOB_{OV}@Fe_x$ catalyst.

Conclusions

In conclusion, 2D disc-shaped OV-rich-BOB nanomaterials were prepared, and further decorated with multi-valent Fe atoms through phytic acid as a bridging molecule. Detailed structural, elemental, and optoelectronic properties of all the as-synthesized materials were investigated, and the results show that the visible light absorption and charge transfer properties are improved by OVs. Furthermore, the presence of Fe atoms affects synergistically by improving the surface adsorption and photo-reduction of the N_2 molecule. This is further supported by photoelectrochemical studies, *i.e.*, transient I–t curves and EIS. These experimental findings are supported by the DFT studies through the optimization of the material's structures and their equilibrium electronic properties (through energy band, TDOS, and PDOS calculations). All the as-synthesized photocatalysts were examined for photocatalytic N_2 fixation to NH_3. The results suggest that due to the synergistic effects of OVs and multivalent Fe atoms, the photocatalytic NH_3 production rate reaches up to 385.5 $\mu M\ g_{cat.}^{-1}\ h^{-1}$ for the optimized photocatalyst, $BOB_{OV}@Fe_5$. The photocatalytic formation of NH_3 has been confirmed by NMR, and further supported by measuring the mass spectra of the indophenol complex. Detailed DFT calculations have been further employed to support the explanation for the photocatalytic performance of the subject material by investigating the energetics of the reaction pathway, and predicting the reaction intermediates. The combined experimental and computational approach successfully elucidates the synergistic effects of Fe doping and OVs in BOB, which will be beneficial for defect engineering and active site modulation in photocatalysts. The results provide useful direction for developing improved photocatalysts and advancing green NH_3 synthesis technologies.

Conflicts of interest

The authors declare no competing financial interest.

Data availability

The data that support the findings of this study are available from the corresponding author(s) upon reasonable request.

Supplementary information (SI): experimental section: chemicals, preparation of the photocatalysts, characterization, photocatalytic N_2 fixation, and computational details. HR-TEM images, EDX spectra, XPS spectra of P 2p, BET isotherms, DRS absorbance spectra, PL & TRPL spectra, standard curves for indophenol and Watt–Chrisp methods, ^{1}H-NMR & HRMS spectra, absorption spectra of indophenol and W–C tests, schematic representation of photocatalytic N_2 reduction, stability study, and XRD patterns, DRS spectra, XPS data of used photocatalyst. Computational NRR mechanism with reaction intermediates involved in alternative pathways of the N_2 reduction reaction on $BOB_{OV}@Fe_x$. See DOI: https://doi.org/10.1039/d5ta06955f.

Acknowledgements

References

1 J. W. Erisman, M. A. Sutton, J. Galloway, Z. Klimont and W. Winiwarter, *Nat. Geosci.*, 2008, **1**, 636–639.
2 J. G. Chen, R. M. Crooks, L. C. Seefeldt, K. L. Bren, R. Morris Bullock, M. Y. Darensbourg, P. L. Holland, B. Hoffman, M. J. Janik, A. K. Jones, M. G. Kanatzidis, P. King, K. M. Lancaster, S. V. Lymar, P. Pfromm, W. F. Schneider and R. R. Schrock, *Science*, 1979, **2018**, 360.
3 R. F. Service, *Science*, 2014, **345**, 610.
4 P. Xia, X. Pan, S. Jiang, J. Yu, B. He, M. Ismail, W. Bai, J. Yang, L. Yang, H. Zhang, M. Cheng, H. Li, Q. Zhang, C. Xiao, Y. Xie, P. F. Xia, X. C. Pan, S. L. Jiang, W. Bai, J. J. Yang, L. Yang, H. H. Zhang, M. Cheng, H. Y. Li, Q. Zhang, C. Xiao, Y. Xie, P. M. Ismail, J. G. Yu and B. W. He, *Adv. Mater.*, 2022, **34**, 2200563.
5 C. Ling, X. Niu, Q. Li, A. Du and J. Wang, *J. Am. Chem. Soc.*, 2018, **140**, 2025.
6 C. Smith, A. K. Hill and L. Torrente-Murciano, *Energy Environ. Sci.*, 2020, **13**, 331–344.
7 X. Zhao, X. Zhang, Z. Xue, W. Chen, Z. Zhou and T. Mu, *J. Mater. Chem. A*, 2019, **7**, 27417–27422.
8 H. Li, J. Shang, Z. Ai and L. Zhang, *J. Am. Chem. Soc.*, 2015, **137**, 6393–6399.
9 G. Dong, T. Zhou, C. Zhang, Y. Wang, Y. Wang, W. Shi, X. Su, T. Zeng and Y. Chen, *ACS Appl. Nano Mater.*, 2024, **7**, 15406–15415.
10 Y. Wei, W. Jiang, Y. Liu, X. Bai, D. Hao and B. J. Ni, *R. Soc. Chem.*, 2022, **14**, 2990–2997.
11 P. Li, Z. Zhou, Q. Wang, M. Guo, S. Chen, J. Low, R. Long, W. Liu, P. Ding, Y. Wu and Y. Xiong, *J. Am. Chem. Soc.*, 2020, **142**, 12430–12439.
12 X. Dong, Z. Cui, X. Shi, P. Yan, Z. Wang, A. C. Co and F. Dong, *Angew. Chem., Int. Ed.*, 2022, **61**, e202200937.
13 G. N. Schrauzer and T. D. Guth, *J. Am. Chem. Soc.*, 1977, **99**, 7189–7193.

14 B. Chang, Y. Guo, H. Liu, L. Li and B. Yang, *J. Mater. Chem. A*, 2022, **10**, 3134–3145.

15 H. Han, Y. Yang, J. Liu, X. Zheng, X. Wang, S. Meng, S. Zhang, X. Fu and S. Chen, *ACS Appl. Energy Mater.*, 2020, **3**, 11275–11284.

16 X. Wang, J. You, Y. Xue, J. Ren, K. Zhang, B. Fu, Q. Xue, J. Tian and H. Zhang, *Appl. Catal., B*, 2025, **363**, 124817.

17 J. Qu, Z. Zhu, X. Xu, J. Lin, Y. Chen, C. Sun, S. Zhu, Z. Fang, M. Jiang and H. Zheng, *Small Methods*, 2025, DOI: 10.1002/smtd.202500493.

18 Y. Liu, W. Wang, S. Zhang, W. Li, G. Wang, Y. Zhang, M. Han and H. Zhang, *ACS Sustain. Chem. Eng.*, 2020, **8**, 2320–2326.

19 C. Zhang, G. Chen, C. Lv, Y. Yao, Y. Xu, X. Jin and Q. Meng, *ACS Sustain. Chem. Eng.*, 2018, **6**, 11190–11195.

20 Z. Zhong, H. J. Zhang, Y. Y. Yang, T. K. Zhang, X. H. Qu, L. Ma, H. L. Cao, Y. D. Hou and J. Lü, *ACS Catal.*, 2025, **15**, 6334–6345.

21 Z. Shen, Z. Luo, J. Chen and Y. Li, *Adv. Funct. Mater.*, 2023, **33**, 2213935.

22 M. Sharma, A. Kumar, D. Gill, S. Jaiswal, A. Patra, S. Bhattacharya and V. Krishnan, *ACS Appl. Mater. Interfaces*, 2023, **15**, 55765–55778.

23 L. Zhang, M. Jiang, H. Tian, S. Liu, X. Zhou, H. Liu, S. Gan, S. Che, Z. Chen, Y. Li, T. Wang, G. Wang and C. Wang, *ACS Sustainable Chem. Eng.*, 2024, **12**, 2028–2040.

24 Y. Fang, Y. Cao, B. Tan and Q. Chen, *ACS Appl. Mater. Interfaces*, 2021, **13**, 42624–42634.

25 J. Hu, Z. Guo, P. E. McWilliams, J. E. Darges, D. L. Druffel, A. M. Moran and S. C. Warren, *Nano Lett.*, 2016, **16**, 74–79.

26 V. K. Sriramadasu and S. Bhattacharyya, *J. Phys. Chem. C*, 2024, **128**, 15286–15297.

27 Y. Liu, Z. Hu and J. C. Yu, *Chem. Mater.*, 2020, **32**, 1488–1494.

28 Y. Zhao, L. Zheng, R. Shi, S. Zhang, X. Bian, F. Wu, X. Cao, G. I. N. Waterhouse and T. Zhang, *Adv. Energy Mater.*, 2020, **10**, 2002199.

29 X. Xue, R. Chen, H. Chen, Y. Hu, Q. Ding, Z. Liu, L. Ma, G. Zhu, W. Zhang, Q. Yu, J. Liu, J. Ma and Z. Jin, *Nano Lett.*, 2018, **18**, 7372–7377.

30 Z. Han, Y. G. Liu, R. Zhang, J. Shi, Y. Jia, X. Liu and H. Y. Jiang, *Langmuir*, 2024, **40**, 15847–15856.

31 V. K. Sriramadasu, B. Kommula, P. Bhardwaj and S. Bhattacharyya, *J. Alloys Compd.*, 2023, **967**, 171814.

32 V. K. Sriramadasu, H. Joshi, S. K. Patro, N. Sharma, A. Singh, S. Pakhira and S. Bhattacharyya, *Small*, 2025, **21**, 2503321.

33 J. Di, C. Chen, C. Zhu, P. Song, J. Xiong, M. Ji, J. Zhou, Q. Fu, M. Xu, W. Hao, J. Xia, S. Li, H. Li and Z. Liu, *ACS Appl. Mater. Interfaces*, 2019, **11**, 30786–30792.

34 X. Li, T. Wang, X. Tao, G. Qiu, C. Li and B. Li, *J. Mater. Chem. A*, 2020, **8**, 17657–17669.

35 Y. Wang, S. Wang, J. Gan, J. Shen, Z. Zhang, H. Zheng and X. Wang, *ACS Sustainable Chem. Eng.*, 2023, **11**, 1962–1973.

36 X. Zheng, X. Wang, L. Feng, Z. Chen, J. Zhang, X. Zhang and P. Liu, *ACS Appl. Mater. Interfaces*, 2024, **16**, 62107–62120.

37 A. Kumar, M. Kumar, V. Navakoteswara Rao, M. V. Shankar, S. Bhattacharya and V. Krishnan, *J. Mater. Chem. A*, 2021, **9**, 17006–17018.

38 Y. Zhang, S. Gu, X. Zhou, K. Gao, K. Sun, D. Wu, J. Xia and X. Wang, *Catal. Sci. Technol.*, 2021, **11**, 4783–4792.

39 X. Xue, R. Chen, C. Yan, Y. Hu, W. Zhang, S. Yang, L. Ma, G. Zhu and Z. Jin, *Nanoscale*, 2019, **11**, 10439–10445.

40 T. Spatzal, K. A. Perez, O. Einsle, J. B. Howard and D. C. Rees, *Science*, 2014, **345**, 1620–1623.

41 W. Du, R. Chen, L. Yang, S. Song, L. Wang, C. Qiu, G. Guan and H. Wan, *Ind. Eng. Chem. Res.*, 2024, **63**, 6201–6209.

42 H. Yang, Y. Huang, B. Luo, Z. Xie, D. Li, D. Xu, Y. Lei and W. Shi, *Chem. Commun.*, 2023, **60**, 1035–1038.

43 Z. Chen, B. Ge, J. Bao, J. Zhang, C. Yuan, H. Xu, W. Yang, Z. Qiu, X. Yang, X. Jiang, X. Wang, J. Zeng, B. Chen and C. Shi, *Inorg. Chem. Front.*, 2024, **11**, 5111–5119.

44 K. Wang, Y. Zhang, L. Liu, N. Lu and Z. Zhang, *J. Mater. Sci.*, 2019, **54**, 8426–8435.

45 Z. Zhang, Y. Zhang, Z. Li, X. Yang, X. Yang, Y. Peng and J. Yu, *Nanomaterials*, 2022, **12**, 1508.

46 D. Channei, B. Inceesungvorn, N. Wetchakun, S. Ukritnukun, A. Nattestad, J. Chen and S. Phanichphant, *Sci. Rep.*, 2014, **4**, 5757.

47 X. Quan, J. Ma, Q. Shao, H. Li, L. Sun, G. Huang, S. Yan, Z. Hong, Y. Wang and X. Wang, *RSC Adv.*, 2024, **14**, 16639–16648.

48 B. Hu, B. H. Wang, L. Chen, Z. J. Bai, W. Zhou, J. K. Guo, S. Shen, T. L. Xie, C. T. Au, L. L. Jiang and S. F. Yin, *ACS Catal.*, 2022, **12**, 11860–11869.

49 X. Feng, Y. Xiao, H. H. Huang, Q. Wang, J. Wu, Z. Ke, Y. Tong and J. Zhang, *Chem.–Asian J.*, 2021, **16**, 3213–3220.

50 X. Wang, X. Shi, S. Yin, P. She, J. Zheng, Y. Song and H. Sun, *J. Mater. Chem. A*, 2023, **11**, 9976–9988.

51 C. Xu, P. Qiu, L. Li, H. Chen, F. Jiang and X. Wang, *ACS Appl. Mater. Interfaces*, 2018, **10**, 25321–25328.

52 H. Wang, Z. Chen, Y. Shang, C. Lv, X. Zhang, F. Li, Q. Huang, X. Liu, W. Liu, L. Zhao, L. Ye, H. Xie and X. Jin, *ACS Catal.*, 2024, **14**, 5779–5787.

53 X. Zheng, H. Han, J. Liu, Y. Yang, L. Pan, S. Zhang, S. Meng and S. Chen, *ACS Appl. Energy Mater.*, 2022, **5**, 4475–4485.

54 M. Ernzerhof and G. E. Scuseria, *J. Chem. Phys.*, 1999, **110**, 5029–5036.

55 R. Puttaswamy, R. Nagaraj, P. Kulkarni, H. K. Beere, S. N. Upadhyay, R. G. Balakrishna, N. Sanna Kotrappanavar, S. Pakhira and D. Ghosh, *ACS Sustainable Chem. Eng.*, 2021, **9**, 3985–3995.

56 H. Joshi, N. Sinha, K. Parveen and S. Pakhira, *Energy Fuels*, 2023, **37**, 19771–19784.

57 A. Erba, J. K. Desmarais, S. Casassa, B. Civalleri, L. Donà, I. J. Bush, B. Searle, L. Maschio, L. Edith-Daga, A. Cossard, C. Ribaldone, E. Ascrizzi, N. L. Marana, J. P. Flament and B. Kirtman, *J. Chem. Theory Comput.*, 2023, **19**, 6891–6932.

58 Q. Geng, H. Xie, W. Cui, J. Sheng, X. Tong, Y. Sun, J. Li, Z. Wang and F. Dong, *J. Phys. Chem. C*, 2021, **125**, 8597–8605.

59 Y. Chen, Q. Sun, X. Tu, L. Chen, W. Han, L. Zhang, X. Duan, M. Liu and H. Zheng, *J. Cleaner Prod.*, 2023, **392**, 136314.

60 Y. Yu, P. Zhang, R. Tuerhong, K. Chai, X. Du, X. Su, L. Zhao and L. Han, *Sep. Purif. Technol.*, 2025, **364**, 132501.